Computerized Medical Imaging and Graphics 68 (2018) 25–39

Contents lists available at ScienceDirect

Computerized Medical Imaging and Graphics

journal homepage: www.elsevier.com/locate/compmedimag

Combined radiogrammetry and texture analysis for early diagnosis of osteoporosis using Indian and Swiss data

Anu Shaju Areeckal[a,*], Jagannath Kamath[b], Sophie Zawadynski[c], Michel Kocher[d], Sumam David S.[a]

[a] Department of Electronics and Communication Engineering, National Institute of Technology Karnataka, Surathkal, Karnataka, India
[b] Department of Orthopedics, Kasturba Medical College, Mangalore, Manipal Academy of Higher Education, Karnataka, India
[c] Nuclear Medicine Service, Hopitaux Universitaires de Geneve (HUG), Geneva, Switzerland
[d] Department of Industrial Technologies, Haute Ecole d'Ingenierie et de Gestion du Canton de Vaud (HEIG-VD), Yverdon-les-Bains, Switzerland

ARTICLE INFO

Keywords:
Osteoporosis
Metacarpal radiogrammetry
Texture analysis
Distal radius

ABSTRACT

Osteoporosis is a bone disorder characterized by bone loss and decreased bone strength. The most widely used technique for detection of osteoporosis is the measurement of bone mineral density (BMD) using dual energy X-ray absorptiometry (DXA). But DXA scans are expensive and not widely available in low-income economies. In this paper, we propose a low cost pre-screening tool for the detection of low bone mass, using cortical radiogrammetry of third metacarpal bone and trabecular texture analysis of distal radius from hand and wrist radiographs. An automatic segmentation algorithm to automatically locate and segment the third metacarpal bone and distal radius region of interest (ROI) is proposed. Cortical measurements such as combined cortical thickness (CCT), cortical area (CA), percent cortical area (PCA) and Barnett Nordin index (BNI) were taken from the shaft of third metacarpal bone. Texture analysis of trabecular network at the distal radius was performed using features obtained from histogram, gray level Co-occurrence matrix (GLCM) and morphological gradient method (MGM). The significant cortical and texture features were selected using independent sample *t*-test and used to train classifiers to classify healthy subjects and people with low bone mass. The proposed pre-screening tool was validated on two ethnic groups, Indian sample population and Swiss sample population. Data of 134 subjects from Indian sample population and 65 subjects from Swiss sample population were analysed. The proposed automatic segmentation approach shows a detection accuracy of 86% in detecting the third metacarpal bone shaft and 90% in accurately locating the distal radius ROI. Comparison of the automatic radiogrammetry to the ground truth provided by experts show a mean absolute error of 0.04 mm for cortical width of healthy group, 0.12 mm for cortical width of low bone mass group, 0.22 mm for medullary width of healthy group, and 0.26 mm for medullary width of low bone mass group. Independent sample *t*-test was used to select the most discriminant features, to be used as input for training the classifiers. Pearson correlation analysis of the extracted features with DXA-BMD of lumbar spine (DXA-LS) shows significantly high correlation values. Classifiers were trained with the most significant features in the Indian and Swiss sample data. Weighted KNN classifier shows the best test accuracy of 78% for Indian sample data and 100% for Swiss sample data. Hence, combined automatic radiogrammetry and texture analysis is shown to be an effective low cost pre-screening tool for early diagnosis of osteoporosis.

1. Introduction

Osteoporosis is a skeletal disorder caused by low bone mass and deterioration of bone structure, resulting in a high susceptibility to fragility fracture of hip, spine and wrist. Osteoporosis is one of the most widespread diseases of the world. It occurs commonly in the elderly population and is more prevalent among women than men (Pande et al., 2006). Being an asymptomatic and painless disease, it is often detected only after occurrence of a fragility fracture. Hence, an early detection of osteoporosis is essential for prevention of osteoporosis-related fractures.

World Health Organization (WHO) recommends measurement of bone mineral density (BMD) using Dual Energy X-ray absorptiometry (DXA) for the diagnosis of osteoporosis. Depending on the *T*-scores,

* Corresponding author.
E-mail addresses: anu_shaju_ec13f06@nitk.edu.in (A.S. Areeckal), jagannath.kamath@gmail.com (J. Kamath), sophie.zawadynski@hcuge.ch (S. Zawadynski), michel.kocher@heig-vd.ch (M. Kocher), sumam@ieee.org (S.D. S.).

https://doi.org/10.1016/j.compmedimag.2018.05.003
Received 11 May 2018; Accepted 18 May 2018

people can be categorized into four categories, namely, Normal for *T*-score ≥ -1, Osteopenia for *T*-score between -1 and -2.5, Osteoporosis for *T*-score ≤ -2.5, and Severe osteoporosis if *T*-score < -2.5 and accompanied with a fragility fracture. Taking as reference the BMD of Caucasian women aged between 20 and 29 years, *T*-score is calculated as the ratio of the difference between estimated BMD and reference BMD to the standard deviation (WHO, 2007). For each increase in standard deviation above or below the mean, *T*-score increases or decreases by 1, respectively.

Although DXA is considered as the gold standard method used for diagnosis of osteoporosis, it suffers from limited availability of DXA machines and high cost of scans in low income economies (IOF, 2013) Cortical radiogrammetry has proved to be a cost effective technique for the detection of bone loss using radiographs (Adami et al., 1996; Anburajan et al., 2001; Barnett and Nordin, 1960; Raheja, 2008; Seo et al., 1994; Shankar et al., 2010; Thodberg et al., 2010; Sam et al., 2017). Digital X-ray Radiogrammetry (DXR) is a computerized cortical radiogrammetric technique being widely explored for the detection of bone diseases like osteoporosis, rheumatoid arthritis, etc. (Böttcher et al., 2004; Rosholm et al., 2001; Ward et al., 2003). However, cortical radiogrammetry measures the cortical bone features alone and does not analyze the trabecular bone texture. The onset of osteoporosis affects the trabecular bone structure before showing a remarkable reduction of cortical bone. Also, the measurement of BMD alone cannot predict the risk of fractures (Mccreadie and Goldstein, 2000). The strength and quality of bone can also be characterized by non-BMD determinants such as micro-architecture of bone. Numerous work have shown the ability of texture analysis of calcaneal trabecular bone in diagnosing osteoporosis and detecting osteoporosis-related fractures (El Hassani et al., 2012; Jennane et al., 2014; Vokes et al., 2010; Yger, 2014). Hence, combining cortical radiogrammetry with texture analysis of trabecular bone can improve the early diagnosis of osteoporosis.

In this paper, we propose a pre-screening tool for detection of low bone mass using cortical radiogrammetry of third metacarpal bone and texture analysis of trabecular bone of distal radius from hand and wrist radiographs. The proposed low cost pre-screening tool can be used for mass screening of people for the detection of low bone mass. For this, a hand and wrist X-ray image of the patient is acquired. The developed software automatically segments the ROIs from which features are extracted and the trained classifier uses these features to classify the patients as healthy or having low bone mass. Those patients detected with low bone mass for further analysis using DXA and other tests.

An automatic segmentation approach to automatically locate and segment the third metacarpal bone shaft and distal radius region of interest (ROI) using mathematical morphological operations and watershed segmentation is proposed. Since osteoporosis is a systemic disease in which bone loss occurs in the whole body, measurement of bone loss in any part of the skeletal body reflects the bone loss at all other parts. Hence, analysis of metacarpal bone and distal radius would be sufficient to detect loss in bone mass. Cortical radiogrammetric measurements are taken from the shaft of third metacarpal bone and bone indices such as combined cortical thickness (CCT), percent cortical area (PCA), Barnett Nordin index (BNI), etc. are calculated. Texture of the trabecular bone of the distal radius ROI is analyzed using texture analysis methods like histogram, gray level co-occurrence matrix (GLCM) and morphological gradient method (MGM). From the extracted cortical and trabecular features, the most significant feature set are selected using independent sample *t*-test and Pearson correlation analysis. This feature set is then used to train different classifiers and tested on each ethnic group.

The remaining paper is organized into the following sections: Section 2 discusses the previous work related to this work, Section 3 describes the data used for this work, Section 4 describes the proposed methodology, Section 5 analyses the results and the scope of this work and finally, Section 6 concludes the main results of the work.

2. Related work

Manual metacarpal radiogrammetry was proposed by Barnett and Nordin (1960). Since then, many bone indices were introduced as a tool to diagnose osteoporosis (Adami et al., 1996; Anburajan et al., 2001; Raheja, 2008; Seo et al., 1994; Thodberg et al., 2010). These work reported the ability of metacarpal radiogrammetric measurements in the diagnosis of osteoporosis. Recently, Sam et al. (2017) showed that cortical radiogrammetry of third metacarpal bone alone can be used to train classifiers for the classification of people with normal and low bone mass. Computerized radiogrammetry, DXR, as a tool to measure BMD was proposed by Rosholm et al. (2001). DXR measures the metacarpal index (MCI) and cortical porosity from second, third and fourth metacarpal bones and uses these measurements to formulate DXR-BMD. DXR-BMD has a good correlation with DXA-BMD, especially at the forearm. However, DXR measures the cortical features alone and does not analyze the structural differences in trabecular bone. This work differs from DXR in the following ways: (1) This work uses the third metacarpal bone alone for cortical radiogrammetry, and (2) it analyses the trabecular texture of the distal radius of wrist and combines it with cortical measurements for the diagnosis.

There are very few publications on trabecular texture analysis of distal radius. Majumdar et al. (2000) analyzed the texture of distal radiographs of healthy and osteoporotic subjects using Fourier power spectrum based fractal analysis and showed that the predictive power of the fractal measures are highly correlated to the trabecular BMD of radial bone. A regression of the trabecular parameters of distal radius radiographs such as spectral, longitudinal and transverse trabecular indices, etc. using neural network is observed to have a better predictive ability of bone strength than DXA-BMD of distal radius Wigderowitz et al. (2000). In their work on the texture analysis of distal radius, Lee et al. (2008) combined fractal, histomorphometric and skeletal texture features with BMD. A sensitivity of 79% and specificity of 66% was obtained using support vector machine (SVM) classifier with leave one out cross validation (LOOCV). Mallard et al. (2013) studied the relationship between distal radius, vertebral and calcaneal radiographic texture analysis and concluded that texture analysis of distal radius provides an early detection of alterations in trabecular microarchitecture.

Since literature on texture analysis of distal radius is limited, we discuss the important work done on calcaneal radiographs in the remaining section. Several papers have reported the potential of trabecular texture features of calcaneal and dental radiographs to classify osteoporotic and healthy subjects. Lespessailles et al. (2008) analyzed calcaneal radiographs using GLCM, run length matrix (RLM) and fractal measures and obtained odds ratio (OR) of 2.72 for fractal parameter (H), OR = 4.78 for BMD and OR = 14.06 for combination of BMD. Vokes et al. (2010) proposed radiographic texture analysis (RTA) features using Fourier analysis and the prevalent OR from logistic regression models were reported. El Hassani et al. (2012) used Dual Tree M-Band wavelet decomposition on projection of images and achieved a high classification accuracy of 98% using calcaneal radiographs. Houam et al. (2014) used one dimensional Local Binary Pattern (LBP) on projections of calcaneal images to obtain an accuracy of 71.3%. Jennane et al. (2014) used statistical measures, GLCM and RLM on calcaneal images after variational model decomposition and achieved a classification accuracy of 85%. Yger (2014) used covariance matrix and wavelet marginals using Haar wavelets in calcaneal radiographs and obtained an accuracy of 74% for covariance matrix and 60% for wavelet marginals. Touvier et al. (2015) obtained OR = 2.07 for trabecular bone score (TBS) and OR = 1.47 for H, on analyzing calcaneal radiographs. Recently, Zheng and Makrogiannis (2016) have used a combination of several texture methods like fractal dimension, wavelet analysis using Haar and Gabor, LBP histogram, Discrete Fourier Transform (DFT), Discrete Cosine Transform (DCT), Laws' masks, edge histogram and GLCM for texture analysis on calcaneal radiographs and

Table 1
Clinical characteristics of the Indian and Swiss sample data groups.

Clinical characteristics	Indian sample data (134 subjects)			Swiss sample data (65 subjects)		
	H (66 subjects) ($\mu \pm \sigma$)	LBM (68 subjects) ($\mu \pm \sigma$)	Significance (p-value)	H (24 subjects) ($\mu \pm \sigma$)	LBM (41 subjects) ($\mu \pm \sigma$)	Significance (p-value)
Age (years)	45.65 ± 10.68	52.75 ± 10.67	1.8E−04‡	70.38 ± 10.11	69.81 ± 8.14	0.8042
Height (cm)	161.24 ± 8.69	157.47 ± 6.12	0.0042†	161.96 ± 11.48	158.32 ± 10.32	0.1927
Weight (kg)	66.71 ± 9.59	58.57 ± 9.36	2.0E−06§	75.58 ± 15.31	67.32 ± 19.95	0.0855
BMI (kg/m^2)	25.74 ± 3.75	23.61 ± 3.46	8.4E−04‡	28.77 ± 4.95	26.74 ± 7.08	0.2205
sBMD (g/cm^2)	1.15 ± 0.12	0.84 ± 0.13	1.5E−28§	1.19 ± 0.34	0.90 ± 0.09	4.4E−06§
T-score	0.07 ± 1.03	-2.55 ± 1.05	2.5E−29§	0.59 ± 2.79	-1.96 ± 0.71	5.5E−07§

$^{*}p < 0.05$, $^{\dagger}p < 0.01$, $^{\ddagger}p < 0.001$, $^{\S}p < 0.0001$.
p-value is determined using independent sample t-test
H – healthy, LBM – low bone mass, BMI – body mass index, sBMD – standard BMD.

achieved a maximum accuracy of 79.3%. Using PCA analysis on histogram and GLCM features extracted from enhanced calcaneal images gave a high accuracy of 96.55% Singh et al. (2017). One-dimensional projections of the calcaneal images were modeled with fractional Brownian motion to calculate the covariance matrix and Rao geodesic distance was used as the distance measure for KNN classifier. Classification accuracy of 96.6% was achieved El Hassouni et al. (2017). Tafraouti et al. (2017) modeled one dimensional projection of band pass filtered images with fractional Brownian motion and obtained classification accuracy of 94.5%. Oulhaj et al. (2017a) proposed a new method, anisotropic discrete dual-tree wavelet transform (ADDTWT), for better characterization of the anisotropic changes in the calcaneal bone and obtained 91.95% accuracy. Circular parametric models were used to characterize trabecular bone texture. Gabor filters along with Wrapped Cauchy model achieved 95.98% accuracy in classifying healthy and osteoporotic cases Oulhaj et al. (2017b). Harrar et al. (2018) combined anisotropic fractional Brownian motion model with anisotropic piecewise Whittle estimator, which showed better performance than other estimators at high frequency with a classification accuracy of 71.8%.

Most of the reported work is done on calcaneal radiographs due to the larger trabecular area and better trabecular texture variations of calcaneal bone as compared to the distal radius. Our motivation to use distal radius for texture analysis is the ease of acquisition and low cost due to analysis of both cortical and trabecular bone from a single hand and wrist radiograph. Also, studies have shown that the distal radius is a potential surrogate site for the assessment of vertebral and hip fractures Wigderowitz et al. (2000), Gomberg et al. (2003).

Our preliminary work on combined radiogrammetry and texture analysis shows that this technique is promising as a pre-screening tool for the classification of healthy subjects and those having low bone mass in Indian population Areeckal et al. (2018a). The objective of the current paper is to validate our proposed methodology in two different population samples, namely Indian and Swiss population and to show that the proposed method can be used as a pre-screening tool across different ethnic groups. We also investigate the use of other texture methods along with cortical features for training different classifiers.

3. Materials used

In this work, sample data from two ethnic groups were used, Indian and Swiss sample populations. Hand and wrist radiographs and DXA-BMD of lumbar spine (DXA-LS) of 134 subjects were acquired from two hospitals in South India. Inclusion criteria was men and women above the age of 30 years and exclusion criteria was pregnant women and subjects under the medication of glucocorticoids in the last three months. The study protocol was approved by the Institutional Ethics Committee, Kasturba Medical College, Mangalore, Manipal Academy of Higher Education, Karnataka, India. The volunteers had given their informed consent. DXA scans of the participants were acquired using GE Lunar densitometer. Images of either left or right hand and wrist with postero-anterior view were obtained either using 400 mA Allengers HF Advantage (deviation index of −2.25 to 3.6) or DR Agfa DX-D 300 (X-ray tube current = 160 mA, X-ray tube voltage = 52 kV, exposure time = 32 ms, source-to-object distance of 990–1370 mm and deviation index of −8.1 to −1.8).

Hand and wrist radiographs and DXA-BMD of lumbar spine of 65 people belonging to Swiss population were analyzed at Centre of Biomedical Imaging (CIBM), University Hospital of Geneva, Geneva, Switzerland. DXA scans of lumbar spine were taken using either Hologic Horizon A or Hologic Discovery A. Thirty hand and wrist X-ray images of patients were acquired using CR Siemens Fluorospot Compact (X-ray tube voltage = 43.8 kV, X-ray tube current from 299 to 329 mA, exposure time from 8 to 11 ms, source to detector distance of 1195–1839 mm and relative X-ray exposure of 205–1005). Twenty-four hand and wrist X-ray images were acquired with Philips Medical Systems DigitalDiagnost (X-ray tube voltage = 52 kV, exposure time from 5 to 10 ms, source to detector distance from 1008 to 1200 mm and relative X-ray exposure of 240–722). The remaining images were acquired using CR Agfa ADC_51xx and DX Agfa DXD30_Wireless with X-ray tube current = 160 mA, X-ray tube voltage = 55 kV and exposure time = 16 ms).

In this work, subjects with T-score ≥ -1 are categorized as healthy (H) group and T-score < -1 are categorized as low bone mass (LBM) group. Data of 66 healthy and 68 low bone mass patients were available in the Indian dataset and 24 healthy and 41 low bone mass patients were available in the Swiss dataset. The clinical characteristics of both the study groups are given in Table 1.

4. Proposed methodology

An automatic radiogrammetric and texture analysis of hand and wrist radiographs for classification of healthy and low bone mass patients is proposed. Automated segmentation and analysis helps to remove subjective error in the measurements and improves the precision and reliability of the technique. The pipeline of the proposed methodology is shown in Fig. 1. It consists of six main stages: (1) Preprocessing, (2) Automatic marker placement and segmentation of third metacarpal bone, (3) Radiogrammetric measurements of cortical bone, (4) Automatic detection of ROI at the distal radius, (5) Texture analysis of trabecular bone and (6) Training classifiers with the extracted features. In stage 1, the input image is denoised and the bone region of hand is extracted using soft tissue subtraction. In stage 2, the third metacarpal bone is located automatically in the hand and wrist radiograph and marker-controlled watershed segmentation is used to detect periosteal (outer) and endosteal (inner) edges of the metacarpal bone. In stage 3, cortical radiogrammetric measurements are determined from the segmented bone shaft. In stage 4, a circular ROI is automatically segmented from distal radius, from which numerous texture features are extracted as described in stage 5. Finally, in stage 6, the

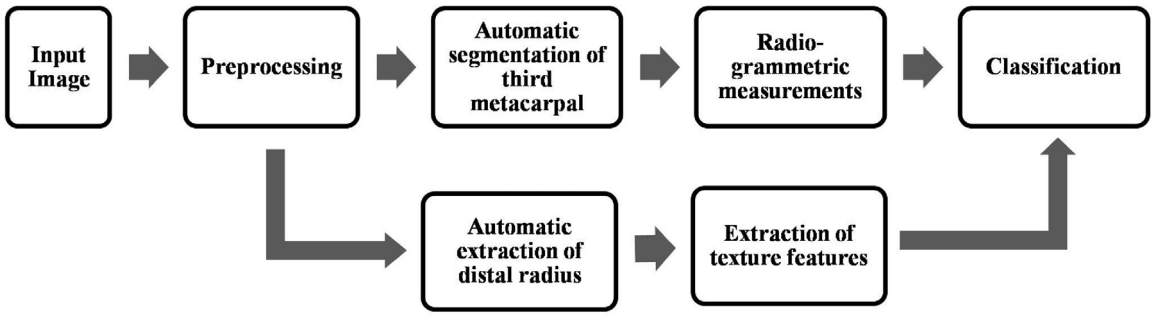

Fig. 1. Outline of the proposed methodology.

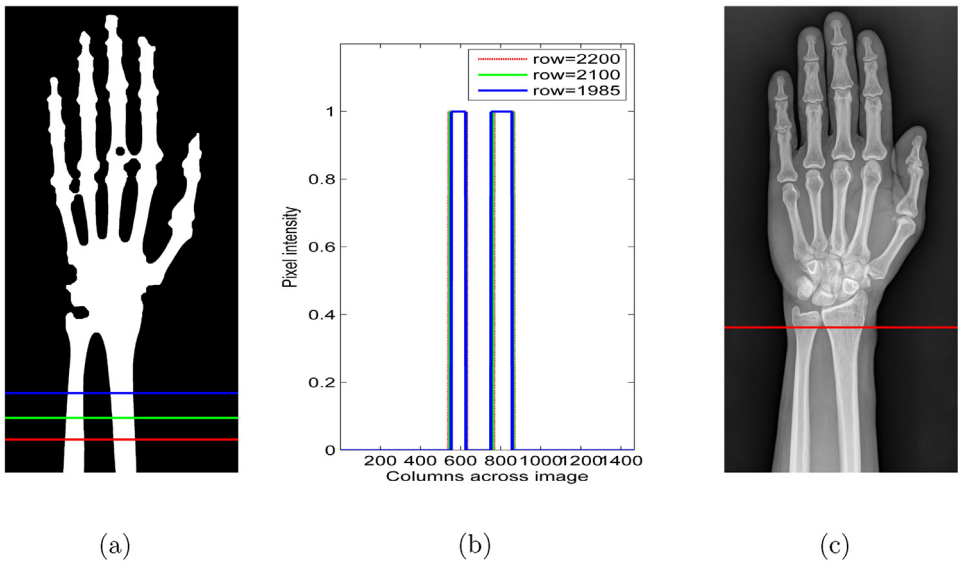

Fig. 2. Detection of DRUJ: (a) and (b) Intensity profiles of radius and ulna showing two distinct peaks, (c) detected DRUJ line.

extracted cortical and trabecular features are statistically analyzed and the most significant features are used for training classifiers.

4.1. Automated segmentation of third metacarpal

The challenges faced by computerized radiogrammetry from radiographs is the noise captured during image acquisition, variation in exposure condition of acquisition and non-uniform illumination, which makes it difficult for using intensity-based region growing algorithms for segmentation. Another difficulty is the close proximity of other metacarpal and carpal bones and low contrast between the bone and soft tissue, making the detection of edges challenging. Hence prior to segmentation, it is necessary to preprocess the hand and wrist images in order to improve the accuracy of segmentation. In this work, the various challenges of X-ray images have been addressed by using denoising, background subtraction and mathematical morphological operations that increases the contrast and edge linking of the hand bones.

Previous work on metacarpal bone segmentation for various applications have used active shape model (ASM), active appearance model (AAM), active feature model, shape particle filters etc. to segment metacarpal bones as they are not intensity-dependent and are robust to illumination variations (Dendere et al., 2013; Fischer, 2009; Langs et al., 2006; Thodberg and Rosholm, 2003). However, these methods require a large number of manually annotated training images for achieving high segmentation accuracy. Our choice of segmentation method is watershed algorithm due to its ease of implementation and good accuracy.

The proposed method for the fully automated segmentation of third metacarpal bone and radiogrammetric measurements have been reported in our previous work Areeckal et al. (2018b). The methodology is discussed below in brief. The hand and wrist image is first linearly mapped to the full dynamic range in order to enhance the contrast of the image. The images are then denoised using Block Matching 3D (BM3D) algorithm that helps to remove both Gaussian and Poisson noise without blurring the edges (Dabov et al., 2007). From the denoised hand and wrist image, the hand bone region is extracted. Non-uniform illumination of the background during data acquisition causes difficulty in producing a good binary and gradient image for the segmentation. This can be alleviated by using large Gaussian filter of standard deviation of 200 pixels to model the background and soft tissue. The estimated background is subtracted from the actual X-ray image to get an image containing hand bones alone. The largest connected component of the binary image is extracted to remove labels and noise at the border and the bounding box of hand bone region is detected.

In order to localize the third metacarpal, mid-region of the metacarpal bone area of the hand is first determined using two reference lines, namely, the horizontal line containing the tip of third distal phalanx (TDP) and the horizontal line containing the Distal Radio-Ulnar Junction (DRUJ). DRUJ is the point of intersection of the radius and ulna bones at the distal end. To detect the DRUJ line, binary image of the background subtracted image is used, which is obtained by combining Otsu's global thresholding and Niblack's local thresholding. DRUJ line is detected from the binary image by taking a series of line profiles in the lower half of the binary image and the line profile with a single peak will denote the point of intersection of the radius and ulna,

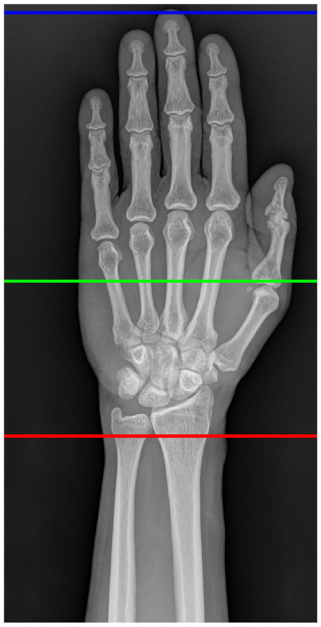

Fig. 3. Image showing the two reference lines (in blue and red) and the estimated metacarpal mid-region (in green). (For interpretation of the references to color in this figure legend, the reader is referred to the web version of the article.)

DRUJ, as shown in Fig. 2. TDP is detected as the upper border of the bounding box of the hand. It is empirically estimated that the midline of the metacarpal region would lie approximately 125 mm below TDP and 70 mm above DRUJ. So the average of these two empirical distances is used to find the metacarpal mid-region. Fig. 3 shows the two reference lines and the detected metacarpal midregion.

A horizontal intensity line taken across the metacarpal mid-region is smoothened by using a zero-phase digital filter to show five prominent peaks, from which the third peak represents the third metacarpal bone, as shown in Fig. 4. As the row line profile obtained is noisy and has many undesired peaks, it is smoothened by using a zero-phase digital filter that filters the row profile in both forward and reverse directions.

The position of the third peak is the centroid of the third metacarpal bone and is used as the internal marker for the watershed segmentation. The central axis of the third metacarpal bone is determined by finding the third most prominent peaks at row profiles 5 mm above and below the centroid in a similar manner. The orientation of the central axis is used to vertically align the third metacarpal bone.

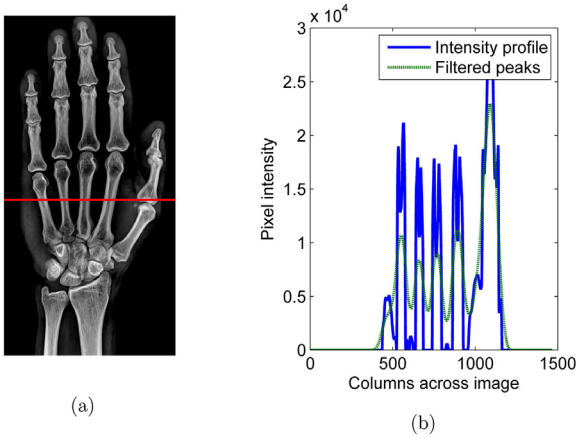

Fig. 4. Localization of third metacarpal bone: (a) Estimated metacarpal mid-region and (b) intensity profile of the soft tissue subtracted image along metacarpal midregion showing five prominent peaks.

The detected centroid of third metacarpal is morphologically dilated by a disk of 2 mm size and used as the internal marker for watershed. A rectangular box surrounding the third metacarpal, with dimensions 45 mm to the top and bottom and 14 mm to the left and right of the centroid, is used as external marker. The gradient image for watershed is obtained by performing a morphological viscous closing of the morphological gradient of the denoised image. The morphological gradient is determined by subtracting the morphologically eroded image from the morphologically dilated image. Watershed segmentation is applied to the gradient image along with the markers to segment the third metacarpal bone, as shown in Fig. 5. Cortical radiogrammetric measurements are taken at the bone shaft of the third metacarpal. The cortical bone shaft is automatically extracted by discarding the metacarpal head and base regions by removing 35% of the upper and lower regions of the segmented metacarpal bone.

For the segmentation of endosteal edge, the segmented periosteal edge is used as external marker and the central axis along the third metacarpal bone shaft is used as the internal marker. Gradient image used for the watershed is obtained by further background subtraction using Gaussian filter of standard deviation 10 pixels to get the cortical bone alone, contrast enhancement of the resulting image and taking the morphological gradient of this image. Marker-controlled watershed results in a proper detection of the endosteal edge. Fig. 6 shows the markers and watershed lines created along the endosteal edge. The radiogrammetric measurements of the cortical bone is taken from the segmented third metacarpal bone.

4.2. Cortical radiogrammetry

Cortical radiogrammetry is a technique by which geometrical measurements are taken from the cortical bone. Metacarpal radiogrammetry takes measurements from the metacarpal bones, usually the second metacarpal bone or the middle three metacarpals together. Bone indices developed from these measurements can be used to measure bone loss in people (Thodberg et al., 2010). In this work, third metacarpal bone shaft is automatically segmented from hand radiographs and radiogrammetric measurements are taken, as shown in Fig. 7.

The different measurements that can be taken from the metacarpal bone shaft are cortical width (CW), medullary width (MW) and cortical area (CA). Cortical width is the total diameter of the bone, measured by finding the average distance between periosteal edges. Medullary width is the diameter of the medullary cavity, corresponding to the average distance between endosteal edges. Here, the cortical and medullary width measurements are taken along 100 positions along the bone shaft and the sum is divided by 100 to get the average CW and MW values. The measurements are determined in number of pixels and converted to units in mm using the pixel dimension determined from DICOM image header file. The difference between the cortical and medullary widths gives the cortical thickness. Cortical area is determined by the area covered by the cortical bone. The bone indices derived from these measurements in order to measure bone loss are combined cortical thickness (CCT), Barnett-Nordin Index (BNI) and percent cortical area (PCA), as given in the equations below.

$$\mathrm{CCT} = \mathrm{CW} - \mathrm{MW} \tag{1}$$

$$\mathrm{BNI} = \frac{\mathrm{CCT}}{\mathrm{CW}} \times 100 \tag{2}$$

$$\mathrm{PCA} = \frac{\mathrm{CW}^2 - \mathrm{MW}^2}{\mathrm{CW}^2} \times 100 \tag{3}$$

4.3. Automatic segmentation of distal radius

Distal radius is a good site for measurement of the trabecular features as the trabeculae fibres are distinctly visible. But the segmentation

(a) (b) (c)

Fig. 5. Automatic segmentation of third metacarpal bone: (a) Internal and external markers for watershed, (b) gradient image, and (c) segmented third metacarpal bone.

of the radius bone is difficult due to its intersection with the ulna and close proximity to the carpal bones. Hence, in this work, the segmentation of distal radius ROI is done by taking the previously detected DRUJ line as reference and using intensity profiles, to approximate the centre and radius of the largest circle that fits into the distal radius, as described in our previous paper Areeckal et al. (2018a). For this, the central axis of the radius bone is first determined by taking three horizontal intensity profiles below DRUJ and determining the location of the wider peaks corresponding to the radius bone. The radius bone is then vertically aligned by finding the orientation of the central axis, similar to the vertical alignment of the third metacarpal bone, as discussed in section 4.1. The DRUJ line is then used as a reference to detect the circular ROI. A horizontal intensity profile is taken 3 mm below the DRUJ line and this profile gives the width of the distal radius, from which the centre and radius of the circular ROI can be approximated. The centre of the circular ROI is estimated as the location of the wider peak (second peak in case of left hand) and the radius of the circular ROI is half the width of this peak. In order to ensure that the detected circle is the largest circle that fits into the distal end of radius bone, a vertical intensity profile is taken from the estimated centre to 20 mm above and the most prominent peak is detected, as shown in Fig. 8. This peak represents the ultra-distal end of the radius bone. By estimating the distance of the centre from the ultra-distal end, the centre is re-adjusted and the circular ROI is extracted, as shown in Fig. 9. After segmentation of the circular ROI, the largest square region inscribed in the circular ROI is extracted and the texture of trabecular bone is analyzed.

4.4. Trabecular texture analysis

Trabecular bone has a honey-comb like structure, which becomes more porous and less connected with progression of osteoporosis. Trabecular bone structure can be characterized using various statistical and structural texture analysis methods. This work uses first order features like histogram features, second order statistical features like gray level co-occurrence matrix (GLCM) and morphological gradient method (MGM) to analyze the trabecular texture of the distal radius of wrist.

The extracted square region of distal radius is first pre-processed in order to characterize the trabecular bone texture more distinctly. The

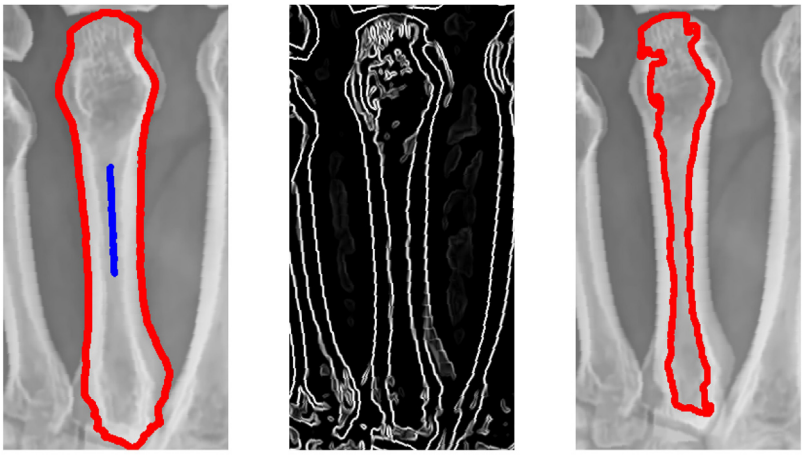

(a) (b) (c)

Fig. 6. Segmentation of endosteal edge: (a) Internal and external markers used for watershed, (b) gradient of the contrast enhanced image, and (c) detected endosteal edge after watershed segmentation.

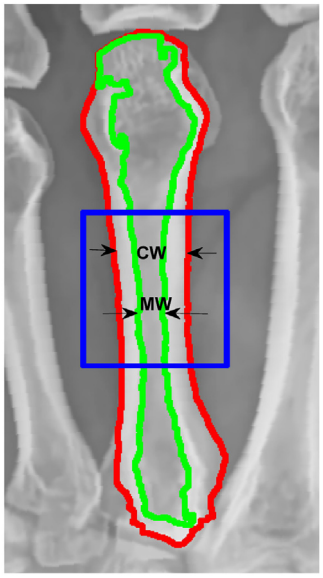

Fig. 7. Detected outer and inner edges and metacarpal shaft for radiogrammetric measurements.

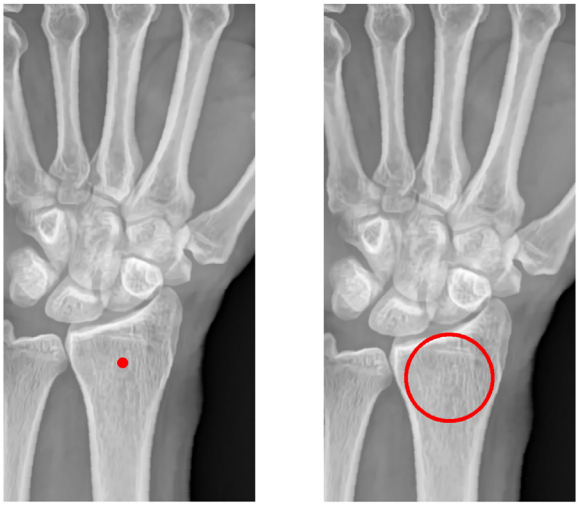

Fig. 9. Extraction of distal radius ROI: (a) Estimation of centre of the circle and (b) extraction of the circular ROI of distal radius.

extracted ROI is resized to 170 × 170 pixels using bicubic interpolation for a uniform texture analysis across the datasets. Pixel intensities are linearly mapped to the full dynamic range. In order to remove the effects of non-uniform illumination and improve the contrast between trabeculae and background, background subtraction is applied to the ROI using Gaussian filter of standard deviation of 50 pixels.

Each of the texture analysis methods discussed below are then used for feature extraction from the ROI images.

4.4.1. Histogram features

Histogram features measure the global characteristics of the image. The histograms of the raw images of healthy and osteoporotic subjects do not show a distinct separation. After extracting the trabecular network using background subtraction, the histogram of healthy subjects show a distinct peak at the higher intensities, while the osteoporotic histogram peaks tend to move towards the lower intensities. This is as expected since the osteoporotic subjects will have less dense and more porous trabecular network. The features extracted from histogram are variance, skewness and kurtosis. Variance measures the average deviation of the histogram values from the mean. Skewness is the measure of the asymmetry of a histogram. If the histogram has more pixels with lower intensities, skewness is negative, and vice versa. Kurtosis characterizes how peaked (positive kurtosis) or flat (negative kurtosis) the distribution is. The equations used for calculating the first order features are given below. The features extracted are abbreviated as $Hist_{var}$, $Hist_{skew}$ and $Hist_{kurt}$ for variance, skewness and kurtosis of the histogram, respectively.

$$\text{Variance, } \sigma^2 = \sum_i \left(\frac{X_i - \overline{X}}{n}\right)^2 \tag{4}$$

$$\text{Skewness} = \frac{\sum_i \left(\frac{X_i - \overline{X}}{\sigma}\right)^3}{n} \tag{5}$$

$$\text{Kurtosis} = \frac{\sum_i \left(\frac{X_i - \overline{X}}{\sigma}\right)^4}{n} - 3 \tag{6}$$

where, X_i is the data point, $\overline{X}$ is the mean and n is the number of data points.

4.4.2. Gray level co-occurrence matrix (GLCM)

Histogram features discussed above does not give information on the relative position of the pixels. GLCM are second order statistical features that exploit the spatial relationship of image pixels on a fixed

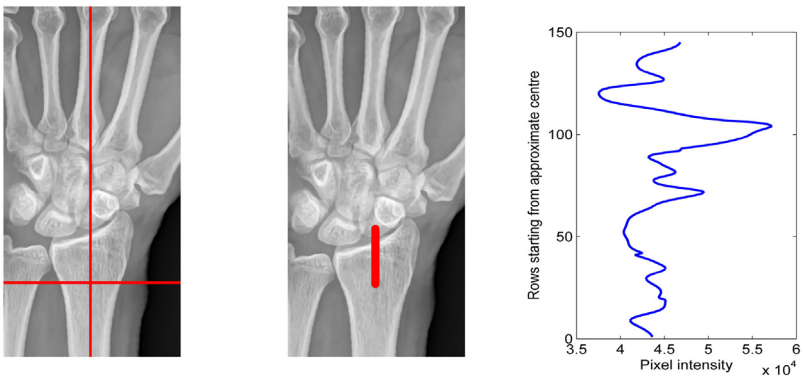

Fig. 8. Estimating the upper boundary of distal radius: (a) Detection of central axis of the radius bone after alignment, (b) shows a vertical line taken from the DRUJ row to a predetermined distance along the central axis and (c) intensity profile along the vertical line in (b) showing the upper boundary as the highest peak.

scale. GLCM defines how many times a pixel intensity co-occurs with another given pixel intensity within a specific distance and direction (Haralick, 1979). In this work, the images were quantized to 256 gray levels for higher contrast and GLCM was calculated. The co-occurrence between pixel pairs at a distance of $d = 1$, 5 and 10 pixels along four directions (0^0, 45^0, 90^0 and 135^0) were determined. The distance was fixed to be 10 as it showed the best results.

The features extracted from the GLCM matrices are energy, homogeneity, contrast, correlation and entropy. If i and j are the row and column positions in the image and $p(i, j)$ represents the matrix element at row i and column j, the features extracted are given by the following equations.

$$\text{Energy} = \sum_{i,j} p(i,j)^2 \tag{7}$$

$$\text{Homogeneity} = \sum_{i,j} \frac{p(i,j)}{1+|i-j|} \tag{8}$$

$$\text{Contrast} = \sum_{i,j} |i-j|^2 p(i,j) \tag{9}$$

$$\text{Correlation} = \sum_{i,j} \frac{(i-\mu_i)(j-\mu_j)p(i,j)}{\sigma_i \sigma_j} \tag{10}$$

$$\text{Entropy} = \sum_{n} k(n) \times \log_2 k(n) \tag{11}$$

where $p(i, j)$ is the matrix element value along ith row and jth column, μ_i, σ_i, μ_j and σ_j are the mean and standard deviation along ith row and jth column respectively. k denotes the total number of counts in bin n of the image histogram.

The total features extracted from GLCM at a distance of 10 pixels are $GLCM_{0_{en}}$, $GLCM_{0_{hom}}$, $GLCM_{0_{cont}}$ and $GLCM_{0_{corr}}$ for energy, homogeneity, contrast and correlation features of the GLCM calculated at orientation 0^0 to the horizontal. Similarly, $GLCM_{45_{en}}$, $GLCM_{45_{hom}}$, $GLCM_{45_{cont}}$ and $GLCM_{45_{corr}}$ denotes the GLCM features at orientation 45^0, $GLCM_{90_{en}}$, $GLCM_{90_{hom}}$, $GLCM_{90_{cont}}$ and $GLCM_{90_{corr}}$ denotes the GLCM features at orientation 90^0 and $GLCM_{135_{en}}$, $GLCM_{135_{hom}}$, $GLCM_{135_{cont}}$ and $GLCM_{135_{corr}}$ denotes the GLCM features at orientation 135^0 to the horizontal.

4.4.3. Morphological gradient method (MGM)

The use of mathematical morphology for texture analysis was introduced by Werman and Peleg (1984). Each mathematical morphological operation is defined with a structuring element, whose size, shape and orientation can enhance different aspects of the image texture. The basic mathematical operations, erosion and dilation, can be used to extract features that are invariant under linear grayscale transformations (Veenland, 1999).

Morphological gradients with different structuring elements are constructed and combined into ratios, as shown below.

$$g = (f \oplus b) - (f \ominus b) \tag{12}$$

$$GR_i = \frac{\sum\sum gs_{i,i}(x,y) - \sum\sum gc_i(x,y)}{\sum\sum gs_{i,i}(x,y) + \sum\sum gc_i(x,y)} \tag{13}$$

$$GSS_{i,j} = \frac{\sum\sum gs_{i,i}(x,y) - \sum\sum gs_{j,j}(x,y)}{\sum\sum gs_{i,i}(x,y) + \sum\sum gs_{j,j}(x,y)} \tag{14}$$

$$GSR_{i,j} = \frac{\sum\sum gc_i(x,y) - \sum\sum gc_j(x,y)}{\sum\sum gc_i(x,y) + \sum\sum gc_j(x,y)} \tag{15}$$

where $gs_{i,j}$ is defined as the gradient image constructed using a rectangular structuring element of size $i \times j$, and gc_i is the gradient image resulting from using a disk structuring element of radius i. The intensity values of the gradient images are summed up and various features such as GR_i, $GSS_{i,j}$ and $GSR_{i,j}$ are extracted, as given in the equations.

The feature GR_i is sensitive to the roundness of the edges, while $GSS_{i,j}$ and $GSR_{i,j}$ assess the size of the edges of the structure. In this work, GR_i was calculated for $i = 5$ and 7. The features $GSS_{i,j}$ and $GSR_{i,j}$ were determined for $i = 7$, 9, 11 and $j = 3$, 5, 7. Veenland (1999) have reported that these parameters give the best results in characterizing the trabecular bone texture. Thus, the total features extracted using MGM are GR_5 and GR_7 for $i = 5$ and 7, $GSS_{7,3}$, $GSS_{9,5}$, $GSS_{11,7}$ representing the feature $GSS_{i,j}$ with ($i = 7$, $j = 3$), ($i = 9$, $j = 5$) and ($i = 11$, $j = 7$), respectively and $GSR_{7,3}$, $GSR_{9,5}$, $GSR_{11,7}$ representing the feature $GSR_{i,j}$ with ($i = 7$, $j = 3$), ($i = 9$, $j = 5$) and ($i = 11$, $j = 7$).

4.4.4. Local binary pattern (LBP)

Local binary pattern (LBP) is a popular texture analysis method being widely used in various applications (Ojala et al., 2002). LBP combines both statistical and structural texture features to capture the local texture information. LBP is obtained by encoding the centre pixel by thresholding the neighborhood of each pixel with the centre value. In this work, rotation-invariant LBP features are extracted and LBP histogram is formed. The features derived from LBP histogram are mean, variance, skew, kurtosis and energy, which are denoted as LBP_{mean}, LBP_{var}, LBP_{skew}, LBP_{kurt} and LBP_{en}.

Local line binary pattern (LLBP) is a relatively recent texture method, used for object recognition and segmentation in medical images (Petpon and Srisuk, 2009). In LLBP, binary encoding is done in the horizontal and vertical directions, in contrast to conventional LBP which encodes the binary pattern of the square neighbourhood. As the trabeculae of the vertically aligned distal radius region appears as almost linear structures, LLBP could extract features that can best capture the texture of trabecular bone. We extract both LBP and LLBP features and show that LLBP helps in better classification as compared to LBP. The horizontal and vertical variants of the LLBP are also separately analyzed to capture directional information. Hence, the mean, variance, skew, kurtosis, energy and entropy of LLBP ($LLBP_{mean}$, $LLBP_{var}$, $LLBP_{skew}$, $LLBP_{kurt}$, $LLBP_{en}$ and $LLBP_{ent}$), horizontal LLBP ($LLBP_{Hor_{mean}}$, $LLBP_{Hor_{var}}$, $LLBP_{Hor_{skew}}$, $LLBP_{Hor_{kurt}}$, $LLBP_{Hor_{en}}$ and $LLBP_{Hor_{ent}}$) and vertical LLBP ($LLBP_{Vert_{mean}}$, $LLBP_{Vert_{var}}$, $LLBP_{Vert_{skew}}$, $LLBP_{Vert_{kurt}}$, $LLBP_{Vert_{en}}$ and $LLBP_{Vert_{ent}}$) are extracted.

4.5. Feature selection and classification

All the described cortical and texture features are combined to a single feature set, which may contain insignificant features. It is essential to discard the unnecessary features as they may reduce the accuracy of classification and increase the complexity of the classifier. Various feature selection methods are available to determine the most dominant and significant features. Here, feature selection is done using independent sample t-test. Features with a significance value, $p < 0.05$, are considered to be significant. The most significant features are selected for training classifiers.

Correlation of the significant features with BMD is determined using Pearson correlation. BMD of Indian and Swiss sample population was obtained from GE Lunar densitometer (BMD_{Lunar}) and Hologic densitometer ($BMD_{Hologic}$), respectively. As BMD was measured from DXA machines of different manufacturers, the values obtained are different, due to differences in ROI, calibration standards and algorithms used for calculation of BMD (Lu et al., 2001). To perform comparison of BMD values between different densitometers, a standard BMD (sBMD) is used and conversion formulas specific to anatomical sites are available. For correlation analysis, the BMD values of lumbar spine are converted to sBMD, using the equations given below (Hui et al., 1997).

$$\text{sBMD} = 0.9683\ (\text{BMD}_{\text{Lunar}} - 1.100) + 1.0436 \tag{16}$$

$$\text{sBMD} = 1.0550\ (\text{BMD}_{\text{Hologic}} - 0.972) + 1.0436 \tag{17}$$

The different classifiers used are logistic regression classifier,

support vector machine (SVM) with a Gaussian kernel and weighted K-nearest neighbor (KNN) classifier. A Gaussian kernel of scale 3.5 is used for the SVM classifier. For KNN, 10 nearest neighbours were considered, with Euclidean distance metric and a squared inverse distance weight. A 10-fold cross-validation (CV) was done due to the small number of training samples used. The performance of the trained classifiers is evaluated using metrics derived from the confusion matrix. A confusion matrix categorizes the obtained output results as true positive (*TP*), false positive (*FP*), true negative (*TN*) and false negative (*FN*). Healthy group is taken as negative class and LBM group is taken as positive class. The performance metrics used in this work are sensitivity (*Sn*), specificity (*Sp*), positive predictive value (*PPV*), negative predictive value (*NPV*), accuracy (*Acc*) and *F*1-score, given by the following equations.

$$\mathrm{Sn} = \frac{\mathrm{TP}}{\mathrm{TP} + \mathrm{FN}} \tag{18}$$

$$\mathrm{Sp} = \frac{\mathrm{TN}}{\mathrm{TN} + \mathrm{FP}} \tag{19}$$

$$\mathrm{PPV} = \frac{\mathrm{TP}}{\mathrm{TP} + \mathrm{FP}} \tag{20}$$

$$\mathrm{NPV} = \frac{\mathrm{TN}}{\mathrm{TN} + \mathrm{FN}} \tag{21}$$

$$\mathrm{Acc} = \frac{\mathrm{TP} + \mathrm{TN}}{\mathrm{TP} + \mathrm{FP} + \mathrm{TN} + \mathrm{FN}} \tag{22}$$

$$F1\text{-}score = \frac{2 \times \mathrm{TP}}{2 \times \mathrm{TP} + \mathrm{FP} + \mathrm{FN}} \tag{23}$$

5. Results and discussion

5.1. Automatic segmentation results

The third metacarpal bone was automatically detected by using two anatomical landmarks (TDP and DRUJ) and intensity profile. Marker-based watershed segmentation was used to control the water filling technique, by avoiding the effect of local minima and thus preventing over-segmentation. Using edge linking on the gradient image ensured proper detection of the edges. As for the segmentation of distal radius ROI, two anatomical landmarks were used, namely the DRUJ and the upper boundary of the radius bone. Use of intensity profiles to locate the bones increased the robustness of the method to illumination variations in images.

The proposed segmentation approach was applied on 134 hand and wrist images of Indian and 65 images of Swiss sample population. The method shows 86% accuracy in detecting the third metacarpal bone and 90% accuracy in extracting the distal radius ROI. Examples of the segmentation results using the proposed approach are shown in Fig. 10.

Ground truth for cortical measurements of six healthy and eight low bone mass category images were provided by experts. Comparison of our proposed automatic radiogrammetry to the ground truth showed a mean absolute error of 0.04 mm (0.51%) for cortical width of the healthy group and 0.12 mm (1.54%) for that of the low bone mass group. A mean absolute error of 0.22 mm (5.81%) and 0.26 mm (7.86%) were obtained for medullary width measurements of the healthy and low bone mass groups, respectively. Table 2 shows the validation results of the proposed automatic radiogrammetric method with the ground truth. Cortical width measurements showed more accuracy than medullary width, due to the presence of a clear demarcation of the outer edge after background subtraction, whereas in the case of medullary width measurements, the contrast between the endosteal edge and soft tissue is low in most cases.

The proposed approach failed to detect the third metacarpal and distal radius ROI in some images due to wrong detection of DRUJ and due to the close proximity of other metacarpal bones. The failed images were semi-automatically segmented by manually selecting the centre of third metacarpal and DRUJ line, and then using these reference lines to automatically segment the ROIs. The semi-automatically segmented images were combined with automatically segmented images for feature extraction. This was done in order to utilize the whole dataset for classification process.

5.2. Classifiers trained with statistical and structural features

In this paper, we develop a computer-aided screening tool that can be used for detection of low bone mass. Statistical and structural texture features of the distal radius are combined with metacarpal radiogrammetry to detect people with low bone mass. Histogram features, GLCM and MGM features extracted from the background subtracted images are used to form one set of texture features to train the classifiers. LBP features extracted directly from the original image without background subtraction forms another set of features. We perform a comparison of the classifiers trained with the two different texture feature sets. In this subsection, we discuss about the classifiers trained with the first set of features, namely histogram features, GLCM and MGM features.

5.2.1. Feature selection

Bone features extracted from both the sample population were analysed for statistical significance and correlation with DXA-LS. The most significant features that were common to both the sample population were selected as the feature set used for classification. Different classifiers were trained on a training set of the Indian sample population with a 10-fold cross validation and tested on unseen images of both the Indian and Swiss sample population.

The discrimination ability of the extracted features was analyzed using independent sample *t*-test. The *t*-tests were tested on the Indian and Swiss sample data separately. Table 3 shows the t-test results with significance values for all features extracted for Indian sample population and Swiss sample population, respectively.

The correlation of the extracted features with sBMD and *T*-score was analyzed using Pearson correlation. Table 4 shows the correlation values of the extracted features with sBMD and *T*-score for Indian and Swiss sample population, respectively. All the cortical features show a very good correlation with $p < 0.0001$. Texture features derived from MGM also shows a very high correlation with $p < 0.001$. The highest correlated feature with sBMD and *T*-score is CCT for both ethnic groups.

Feature selection for training the classifiers was done using the results of *t*-test. The features common to significant features of Indian data ($p < 0.01$) and significant features of Swiss data ($p < 0.01$) were selected. The 28 features thus selected are *CCT*, *CA*, *PCA*, *BNI*, $Hist_{skew}$, $Hist_{kurt}$, $GLCM_{0_{cont}}$, $GLCM_{0_{hom}}$, $GLCM_{0_{en}}$, $GLCM_{45_{cont}}$, $GLCM_{45_{hom}}$, $GLCM_{45_{en}}$, $GLCM_{45_{ent}}$, $GLCM_{90_{hom}}$, $GLCM_{90_{en}}$, $GLCM_{90_{ent}}$, $GLCM_{135_{cont}}$, $GLCM_{135_{hom}}$, $GLCM_{135_{en}}$, $GLCM_{135_{ent}}$, GR_5, GR_7, $GSS_{7,3}$, $GSS_{9,5}$, $GSS_{11,7}$, $GSR_{7,3}$, $GSR_{9,5}$, $GSR_{11,7}$.

5.2.2. Performance of trained classifiers

The Indian sample data was partitioned into training set of 120 images with 60 images each from healthy and low bone mass groups, and a test set of 14 unseen images. A 10-fold cross validation was done on the training set. All data of the Swiss sample population was used for testing the trained classifiers. The features of the training set were normalized with zero mean and unit variance prior to training the classifiers. The trained classifiers were evaluated with confusion matrices. Table 5 shows the performance metrics of the classifiers using 10-fold cross validation. SVM shows better performance on cross validation as compared to logistic regression and KNN classifiers.

Table 6 shows the cross-validation accuracy and test accuracy of the trained classifiers. Performance of the classifiers on cortical features alone (*CCT*, *CA*, *PCA*, *BNI*), texture features alone ($Hist_{skew}$, $Hist_{kurt}$,

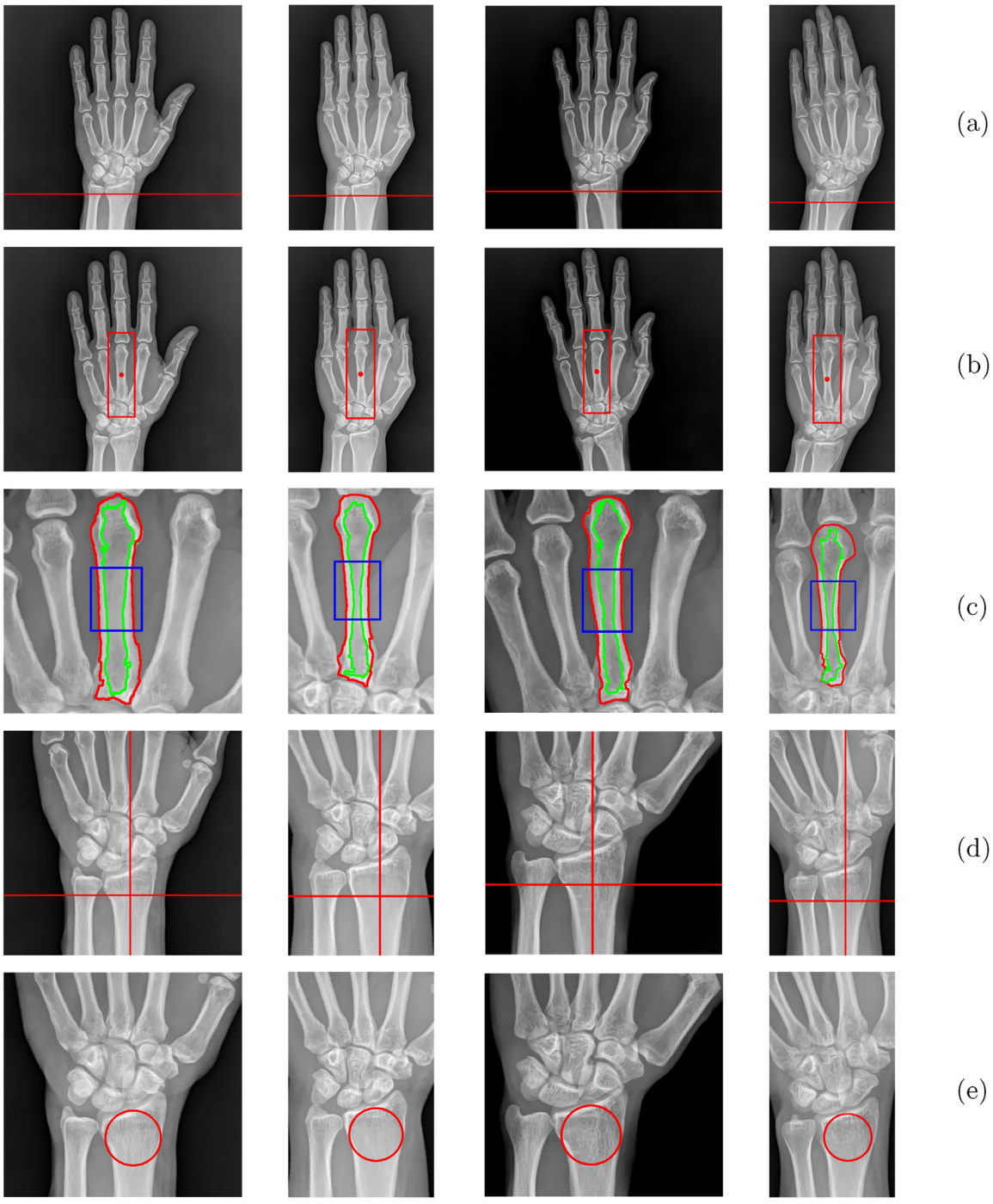

Fig. 10. Examples of the segmentation results for radiogrammetry for two healthy images (left) and two osteoporotic images (right): (a) Original images with detected distal radius-ulnar junction (DRUJ) line are shown in first row, (b) localization of third metacarpal in second row, (c) segmented third metacarpal bone shaft in third row, (d) detected central axis and approximate centre of circular distal radius ROI in fourth row, and (e) the extracted circular ROI in the last row.

$GLCM_{0_{cont}}$, $GLCM_{0_{hom}}$, $GLCM_{0_{en}}$, $GLCM_{45_{cont}}$, $GLCM_{45_{hom}}$, $GLCM_{45_{en}}$, $GLCM_{45_{ent}}$, $GLCM_{90_{hom}}$, $GLCM_{90_{en}}$, $GLCM_{90_{ent}}$, $GLCM_{135_{cont}}$, $GLCM_{135_{hom}}$, $GLCM_{135_{en}}$, $GLCM_{135_{ent}}$, GR_5, GR_7, $GSS_{7,3}$, $GSS_{9,5}$, $GSS_{11,7}$, $GSR_{7,3}$, $GSR_{9,5}$, $GSR_{11,7}$) and combined cortical and texture features are shown in the table. It can be observed that combining cortical and texture features help to improve the performance of the classifiers in terms of the test accuracy on unseen data. Weighted KNN shows the best test accuracy of 78% on Indian test data and 100% on Swiss sample data.

5.3. Classifiers trained with LBP features

This section discusses about the performance of classifiers trained with LBP features. LBP texture methods used in this work are rotation-invariant LBP, local line binary pattern (LLBP), and its horizontal and vertical variants. LBP with the adjacent neighbourhood of 8 neighbours were extracted. For LLBP and its variants, a line of length 17 pixels was found to give good results.

5.3.1. Feature selection

From the extracted LBP features and its variants, the features that

Table 2
Comparison of radiogrammetric measurements with ground truth.

Images	Ground truth		Proposed method			
	Actual CW (mm)	Actual MW (mm)	Measured CW (mm)	Absolute error (mm)	Measured MW (mm)	Absolute error (mm)
Healthy						
1	8.75	4.19	8.72	0.03	3.54	0.65
2	9.14	4.42	9.04	0.10	4.17	0.25
3	10.45	5.85	10.43	0.02	5.84	0.01
4	8.89	3.98	8.90	0.01	3.75	0.23
5	7.55	2.62	7.51	0.04	2.57	0.05
6	7.72	2.22	7.78	0.06	2.09	0.13
Mean				**0.04**		**0.22**
Low bone mass						
7	6.61	2.89	6.39	0.22	2.36	0.53
8	10.27	4.92	9.96	0.31	4.45	0.47
9	7.94	2.63	7.98	0.04	2.73	0.10
10	7.89	3.18	7.92	0.03	3.27	0.09
11	8.48	4.20	8.34	0.14	4.14	0.06
12	8.44	2.92	8.40	0.04	3.06	0.14
13	6.73	3.17	6.53	0.20	2.50	0.67
14	8.48	4.88	8.48	0.00	4.93	0.05
Mean				**0.12**		**0.26**

were significantly correlated with sBMD of both the ethnic groups were selected for training the different classifiers. Table 7 shows the correlation of the LBP features with sBMD of both Indian and Swiss data samples.

The features that are significantly correlated with sBMD among Indian and Swiss sample data are selected as the input feature set to train the classifiers. Hence, the selected set of texture features are LBP (LBP_{mean}, LBP_{var}, LBP_{skew}, LBP_{kurt}), LLBP ($LLBP_{mean}$, $LLBP_{en}$, $LLBP_{ent}$),

Table 3
Significance test results of healthy (H) and low bone mass (LBM) groups of Indian and Swiss sample populations.

Sl. no	Features extracted	Indian-H ($\mu \pm \sigma$)	Indian-LBM ($\mu \pm \sigma$)	p-value	Swiss-H ($\mu \pm \sigma$)	Swiss-LBM ($\mu \pm \sigma$)	p-value
1	*CCT* (mm)	4.48 ± 0.58	3.90 ± 0.55	8.9E−08§	4.36 ± 0.64	3.75 ± 0.66	5.8E−05§
2	*CA*(mm^2)	43.13 ± 7.28	36.54 ± 6.82	9.1E−07§	41.73 ± 7.97	36.92 ± 8.34	0.0095†
3	*PCA* (%)	78.12 ± 7.21	74.06 ± 7.14	0.0022†	77.21 ± 7.78	70.58 ± 7.25	0.0002‡
4	*BNI*	53.88 ± 7.86	49.55 ± 6.99	0.0016†	52.94 ± 8.12	46.15 ± 6.57	8.8E−05§
5	$Hist_{var}$	1198.73 ± 269.27	1337.80 ± 257.95	0.0041†	1368.90 ± 297.46	1529.85 ± 275.90	0.0136*
6	$Hist_{skew}$	0.67 ± 0.38	0.50 ± 0.23	0.0033†	0.53 ± 0.30	0.35 ± 0.15	0.0009‡
7	$Hist_{kurt}$	1.29 ± 1.51	0.60 ± 0.72	0.0015†	0.67 ± 0.94	0.09 ± 0.44	0.0007‡
8	$GLCM0_{cont}$	1751.99 ± 560.16	2066.26 ± 441.28	0.0007‡	2057.61 ± 640.16	2518.25 ± 566.13	0.0009‡
9	$GLCM0_{corr}$	0.26 ± 0.13	0.21 ± 0.09	0.0231*	0.25 ± 0.12	0.17 ± 0.07	0.0004‡
10	$GLCM0_{hom}$	0.08 ± 0.01	0.07 ± 0.01	0.0002‡	0.07 ± 0.01	0.07 ± 0.01	0.0004‡
11	$GLCM0_{en}$	0.00 ± 0.00	0.00 ± 0.00	0.0003‡	0.00 ± 0.00	0.00 ± 0.00	0.0014†
12	$GLCM0_{ent}$	0.83 ± 0.07	0.87 ± 0.05	0.0008‡	0.86 ± 0.06	0.90 ± 0.05	0.0102*
13	$GLCM45_{cont}$	1908.57 ± 561.49	2238.35 ± 456.93	0.0005‡	2235.06 ± 647.09	2671.11 ± 589.37	0.0022†
14	$GLCM45_{corr}$	0.16 ± 0.10	0.12 ± 0.08	0.0484*	0.15 ± 0.10	0.10 ± 0.07	0.0120†
15	$GLCM45_{hom}$	0.08 ± 0.01	0.07 ± 0.01	0.0002‡	0.07 ± 0.01	0.06 ± 0.01	0.0007‡
16	$GLCM45_{en}$	0.00 ± 0.00	0.00 ± 0.00	0.0003‡	0.00 ± 0.00	0.00 ± 0.00	0.0015†
17	$GLCM45_{ent}$	0.82 ± 0.07	0.86 ± 0.05	0.0007‡	0.85 ± 0.06	0.89 ± 0.05	0.0085†
18	$GLCM90_{cont}$	1475.59 ± 424.57	1648.32 ± 347.83	0.0151*	1713.17 ± 492.76	2114.97 ± 513.82	0.0006‡
19	$GLCM90_{corr}$	0.35 ± 0.09	0.36 ± 0.08	0.7942	0.35 ± 0.09	0.29 ± 0.08	0.0084†
20	$GLCM90_{hom}$	0.09 ± 0.01	0.08 ± 0.01	0.0069†	0.08 ± 0.01	0.07 ± 0.01	0.0003‡
21	$GLCM90_{en}$	0.00 ± 0.00	0.00 ± 0.00	0.0007‡	0.00 ± 0.00	0.00 ± 0.00	0.0010†
22	$GLCM90_{ent}$	0.82 ± 0.07	0.85 ± 0.05	0.0019†	0.85 ± 0.07	0.89 ± 0.05	0.0057†
23	$GLCM135_{cont}$	1873.11 ± 545.16	2218.92 ± 453.76	0.0002‡	2172.25 ± 624.56	2658.90 ± 566.21	0.0004‡
24	$GLCM135_{corr}$	0.17 ± 0.10	0.13 ± 0.08	0.0133*	0.17 ± 0.09	0.09 ± 0.06	9.3E−05§
25	$GLCM135_{hom}$	0.08 ± 0.01	0.07 ± 0.01	9.6E−05§	0.07 ± 0.01	0.06 ± 0.01	6.8E−05§
26	$GLCM135_{en}$	0.00 ± 0.00	0.00 ± 0.00	0.0003‡	0.00 ± 0.00	0.00 ± 0.00	0.0011†
27	$GLCM135_{ent}$	0.82 ± 0.07	0.86 ± 0.05	0.0006‡	0.85 ± 0.06	0.89 ± 0.05	0.0066†
28	GR_5	26.73 ± 2.50	28.40 ± 2.23	0.0001‡	25.27 ± 3.18	23.18 ± 3.41	0.0056†
29	GR_7	23.72 ± 2.66	25.13 ± 2.11	0.0016†	22.69 ± 2.84	20.71 ± 3.07	0.0034†
30	$GSS_{7,3}$	183.55 ± 13.32	192.75 ± 12.26	0.0001‡	174.45 ± 18.72	161.95 ± 20.84	0.0057†
31	$GSS_{9,5}$	106.32 ± 9.66	111.86 ± 8.15	0.0008‡	101.65 ± 11.03	93.52 ± 12.86	0.0031†
32	$GSS_{11,7}$	72.21 ± 7.93	75.81 ± 6.09	0.0056†	69.29 ± 7.97	63.19 ± 9.21	0.0020†
33	$GSR_{7,3}$	205.13 ± 13.73	215.24 ± 12.99	5.3E−05§	194.54 ± 20.92	180.78 ± 22.98	0.0061†
34	$GSR_{9,5}$	114.83 ± 9.66	121.06 ± 8.62	0.0002‡	109.39 ± 11.92	100.84 ± 13.81	0.0038†
35	$GSR_{11,7}$	78.09 ± 7.80	82.26 ± 6.43	0.0016†	74.81 ± 8.30	68.44 ± 9.81	0.0023†

$^{*}p < 0.05$, $^{\dagger}p < 0.01$, $^{\ddagger}p < 0.001$, $^{\S}p < 0.0001$.

Table 4
Correlation analysis of extracted features with sBMD and *T*-score for Indian and Swiss sample populations.

Sl. no	Features extracted	Indian sample population		Swiss sample population	
		sBMD	*T*-score	sBMD	*T*-score
1	*CCT*	0.5133§	0.4806§	0.4773§	0.3974‡
2	*CA*	0.4527§	0.4035§	0.4207§	0.3198†
3	*PCA*	0.3569§	0.3524§	0.3489†	0.3106†
4	*BNI*	0.3595§	0.3560§	0.3625‡	0.3300†
5	$Hist_{var}$	−0.2072*	−0.2158*	−0.3572†	−0.3760‡
6	$Hist_{skew}$	0.2098*	0.2226†	0.5178§	0.4630§
7	$Hist_{kurt}$	0.2270†	0.2363†	0.4923§	0.4429§
8	$GLCM_{0cont}$	−0.2565†	−0.2626†	−0.4658§	−0.4585§
9	$GLCM_{0corr}$	0.2047*	0.2055*	0.4767§	0.4378§
10	$GLCM_{0hom}$	0.2658†	0.2763†	0.4901§	0.4764§
11	$GLCM_{0en}$	0.2577†	0.2686†	0.4534§	0.4458§
12	$GLCM_{0ent}$	−0.2193*	−0.2286†	−0.3867‡	−0.3911‡
13	$GLCM_{45cont}$	−0.2506†	−0.2564†	−0.4324§	−0.4302§
14	$GLCM_{45corr}$	0.1241	0.1244	0.3109†	0.2938†
15	$GLCM_{45hom}$	0.2639†	0.2737†	0.4637§	0.4564§
16	$GLCM_{45en}$	0.2604†	0.2714†	0.4506§	0.4445§
17	$GLCM_{45ent}$	−0.2306†	−0.2401†	−0.3954‡	−0.3995‡
18	$GLCM_{90cont}$	−0.1336	−0.1463	−0.4577§	−0.4732§
19	$GLCM_{90corr}$	−0.1153	−0.1042	0.2999†	0.3149†
20	$GLCM_{90hom}$	0.1407	0.1555	0.4647§	0.4631§
21	$GLCM_{90en}$	0.2358†	0.2489†	0.4625§	0.4576§
22	$GLCM_{90ent}$	−0.2022*	−0.2132*	−0.4111‡	−0.4190§
23	$GLCM_{135cont}$	−0.2828‡	−0.2881‡	−0.4742§	−0.4780§
24	$GLCM_{135corr}$	0.1920*	0.1909*	0.4396§	0.4381§
25	$GLCM_{135hom}$	0.2868‡	0.2953‡	0.5142§	0.5100§
26	$GLCM_{135en}$	0.2664†	0.2775†	0.4635§	0.4566§
27	$GLCM_{135ent}$	−0.2350†	−0.2442†	−0.4060‡	−0.4101‡
28	GR_5	−0.4609§	−0.4354§	0.3201†	0.3193†
29	GR_7	−0.3996§	−0.3750§	0.3494†	0.3579†
30	$GSS_{7,3}$	−0.4476§	−0.4221§	0.3256†	0.3223†
31	$GSS_{9,5}$	−0.4087§	−0.3844§	0.3515†	0.3613‡
32	$GSS_{11,7}$	−0.3736§	−0.3526§	0.3578†	0.3764‡
33	$GSR_{7,3}$	−0.4586§	−0.4322§	0.3187†	0.3122†
34	$GSR_{9,5}$	−0.4348§	−0.4100§	0.3422†	0.3478†
35	$GSR_{11,7}$	−0.3975§	−0.3745§	0.3559†	0.3701‡

$^{*}p < 0.05$, $^{\dagger}p < 0.01$, $^{\ddagger}p < 0.001$, $^{\S}p < 0.0001$.

horizontal LLBP ($LLBP_{Hor_{mean}}$, $LLBP_{Hor_{skew}}$, $LLBP_{Hor_{en}}$, $LLBP_{Hor_{ent}}$) and vertical LLBP ($LLBP_{Vert_{mean}}$, $LLBP_{Vert_{skew}}$). The cortical features used to combine with the texture features are *CCT*, *CA*, *PCA* and *BNI*.

5.3.2. Performance of trained classifiers

Performance of the trained classifiers using 10-fold cross validation on combined cortical and LBP feature variants are shown in Table 8. The best performance metrics are obtained by SVM classifier in LBP, LLBP and vertical LLBP features. Logistic regression classifier shows better results using horizontal LLBP features.

Table 9 shows the test results of the classifiers trained with LBP and LLBP features, combined with cortical radiogrammetric features. We observe that LLBP and its variants show a much better performance than the conventional LBP, and hence the linear descriptor LLBP is a more suitable feature descriptor of the trabecular texture of the bone. The best performance is achieved by weighted KNN trained with vertical LBP features, with a 10-fold CV accuracy of 71%, and test accuracy of 75% and 61% for Indian and Swiss sample data, respectively.

Table 6
Test accuracy of the trained classifiers.

Classifier	Feature set	10 fold CV accuracy	Test accuracy		
			Indian test data	Swiss test data	Overall test data
Logistic regression	Cortical features	70	57	63	62
	Texture features	61	85	70	73
	All features	70	78	73	74
SVM	Cortical features	74	64	67	67
	Texture features	68	64	73	72
	All features	75	78	78	78
KNN	Cortical features	70	71	100	94
	Texture features	69	71	100	94
	All features	73	78	100	96

As seen from Tables 6 and 9, a comparison of the performance of trained classifiers on both sets of features show that the weighted KNN classifier trained with histogram features, GLCM and MGM features show the best overall test accuracy for Indian and Swiss data.

All the image processing techniques and analyses was done using Matlab R2016a and Image Processing, Statistics, Machine Learning and SDC Morphology toolboxes for Matlab Dougherty and Lotufo (2003). The processing time of the diagnostic technique is approximately 1.5 min on a PC with 8GB RAM, 64-bit OS and Intel Core i7-4790 CPU @3.60 GHz. The algorithm is being implemented as executable C codes, which would help in greatly reducing the processing time and can be incorporated into the imaging software. Since the data analysis can be done at no additional equipment cost, it can be a promising low-cost technique for pre-screening of people having low bone mass.

5.4. Comparison with previous work

Related work on trabecular texture analysis of distal radius radiographs and classification is limited, we have compared our classification results with that of classifiers trained on texture analysis of calcaneal radiographs using cross-validation, as shown in Table 10. The work on texture analysis of calcaneal radiographs use manual extraction of ROI with the help of two anatomical landmarks marked by experts.

It can be observed that our results are better than the related work on distal radius radiographs that includes BMD for training the classifier and calcaneal radiographs using fractal analysis, statistical and structural features Lee et al. (2008), Houam et al. (2014), Yger (2014), Zheng and Makrogiannis (2016), Harrar et al. (2018).

5.5. Limitations of the study

This pilot study has been carried out with a sample dataset and needs to be further validated on a larger sample size. The segmentation failed for some images due to binary images having fused radius and ulna bones, resulting in incorrect detection of DRUJ. The accuracy of

Table 5
Performance metrics of the classifiers using 10-fold cross validation on combined cortical and texture (Histogram, GLCM and MGM) features.

Classifier	TP	FP	TN	FN	Sn	Sp	PPV	NPV	Accuracy	*F*1-score
Logistic regression	40	16	44	20	66.67	73.33	71.43	68.75	70.00	68.97
SVM	52	21	39	8	86.67	65.00	71.23	82.98	75.83	78.20
KNN	45	17	43	15	75.00	71.67	72.58	74.14	73.33	73.77

Table 7
Correlation analysis of LBP features with sBMD for Indian and Swiss sample populations.

LBP methods	Features	Indian sample population	Swiss sample population
LBP	LBP_{mean}	0.2231*	0.3285*
	LBP_{var}	0.2182*	0.3305*
	LBP_{skew}	−0.2487†	−0.3348*
	LBP_{kurt}	−0.2625†	−0.3248*
	LBP_{en}	−0.2449†	−0.3073
LLBP	$LLBP_{mean}$	−0.2777†	−0.3581*
	$LLBP_{var}$	0.4805§	0.2169
	$LLBP_{skew}$	0.1659	0.3639*
	$LLBP_{kurt}$	−0.5052§	−0.2720
	$LLBP_{en}$	−0.4918§	−0.3159*
	$LLBP_{ent}$	0.4948§	0.3257*
Horizontal LLBP	$LLBP_{Hormean}$	−0.5273§	−0.3544*
	$LLBP_{Hor_{var}}$	0.0739	−0.2018
	$LLBP_{Hor_{skew}}$	0.5012§	0.3189*
	$LLBP_{Hor_{kurt}}$	−0.2096*	0.0810
	$LLBP_{Hor_{en}}$	−0.4433§	−0.3376*
	$LLBP_{Hor_{ent}}$	0.4401§	0.3449*
Vertical LLBP	$LLBP_{Vert_{mean}}$	−0.3568§	−0.3770*
	$LLBP_{Vert_{var}}$	0.1972*	0.0110
	$LLBP_{Vert_{skew}}$	0.3682§	0.3588*
	$LLBP_{Vert_{kurt}}$	−0.3434§	−0.2684
	$LLBP_{Vert_{en}}$	−0.3143‡	−0.2886
	$LLBP_{Vert_{ent}}$	0.2901‡	0.2808

*$p < 0.05$, †$p < 0.01$, ‡$p < 0.001$, §$p < 0.0001$.

segmentation can be further improved by improving the binarization technique for DRUJ detection. Another reason for failure is the low contrast of some images. Another limitation of the study is the limited dataset available for training of classifiers. Future work includes validation of the work on a larger population sample, and improving the robustness of segmentation algorithm to image contrast in order to increase the segmentation accuracy. Recent texture analysis methods like deep features needs to be investigated with a larger dataset.

6. Conclusion

A cost-effective pre-screening tool has been proposed for the early detection of low bone mass using cortical radiogrammetry of third metacarpal bone and texture analysis of the trabecular bone architecture at the distal radius of wrist. The automatic segmentation approach shows a detection accuracy of 86% in accurately detecting the shaft of third metacarpal bone and 90% in segmenting the distal radius ROI. When the automatic cortical measurements were compared with the ground truth, a mean absolute error of 0.04 mm and 0.12 mm was obtained for cortical width of healthy and low bone mass groups, respectively. A mean absolute error of 0.22 mm and 0.26 mm was obtained for medullary width of healthy and low bone mass groups, respectively. Bone indices like CCT, CA, PCA and BNI were calculated through automatic radiogrammetric measurements. Histogram features, GLCM and morphological gradients method were used for trabecular bone characterization. The cortical and texture features extracted were statistically analysed using independent sample t-test and Pearson correlation. The most significant features common to both Indian and Swiss sample data were selected to train different classifiers. Weighted KNN shows the best performance with a 10-fold CV accuracy of 73% and test accuracy of 78% and 100% for Indian and Swiss test data. Hence, the proposed tool using radiogrammetry and texture analysis of hand and wrist radiographs proves to be a potential low-cost screening tool for early detection of low bone mass.

Table 9
Test accuracy of classifiers trained with LBP features.

LBP method	Classifier	Feature set	10-fold CV accuracy	Test accuracy		
				Indian test data	Swiss test data	Overall test data
LBP	Logistic regression	All features	74	75	58	61
	SVM	All features	75	58	55	56
	KNN	All features	70	58	55	56
LLBP	Logistic regression	All features	77	66	47	50
	SVM	All features	77	58	58	58
	KNN	All features	74	58	65	64
Horizontal LBP	Logistic regression	All features	79	50	60	58
	SVM	All features	73	75	55	58
	KNN	All features	76	66	53	56
Vertical LBP	Logistic regression	All features	73	75	58	61
	SVM	All features	74	66	58	60
	KNN	All features	71	75	61	64

Funding

This data collection was supported by the Technical Education Quality Improvement Program (TEQIP), National Institute of Technology Karnataka (NITK), Surathkal, Karnataka, India.

Table 8
Performance metrics of the classifiers using 10-fold cross validation on combined cortical and LBP feature variants.

Texture features	Classifier	TP	FP	TN	FN	Sn	Sp	PPV	NPV	Accuracy	*F*1-score
LBP	Logistic regression	44	15	45	16	73.33	75.00	74.58	73.77	74.17	73.95
	SVM	50	20	40	10	83.33	66.67	71.43	80.00	75.00	76.92
	KNN	42	18	42	18	70.00	70.00	70.00	70.00	70.00	70.00
LLBP	Logistic regression	48	15	45	12	80.00	75.00	76.19	78.95	77.50	78.05
	SVM	53	20	40	7	88.33	66.67	72.60	85.11	77.50	79.70
	KNN	48	19	41	12	80.00	68.33	71.64	77.36	74.17	75.59
Horizontal LLBP	Logistic regression	49	14	46	11	81.67	76.67	77.78	80.70	79.17	79.67
	SVM	45	17	43	15	75.00	71.67	72.58	74.14	73.33	73.77
	KNN	47	15	45	13	78.33	75.00	75.81	77.59	76.67	77.05
Vertical LLBP	Logistic regression	44	16	44	16	73.33	73.33	73.33	73.33	73.33	73.33
	SVM	53	24	36	7	88.33	60.00	68.83	83.72	74.17	77.37
	KNN	45	19	41	15	75.00	68.33	70.31	73.21	71.67	72.58

Table 10
Comparison of performance metrics of classifiers trained on bone radiographic texture analysis in literature.

Sl no.	Texture features	ROI (Segmentation)	Dataset	Classifier	Sn	Sp	PPV	NPV	Accuracy	*F*1-score	Reference
1	Wavelet Marginals-Haar	Calcaneal (Manual)	58 cases &58 controls	SVM	62.1	65.5	64.3	63.3	63.8	63.2	Yger (2014)
2	1D LBP	Calcaneal (Manual)	39 cases &41 controls	KNN	–	43.9	–	–	71.3	77.2	Houam et al. (2014)
3	Fractal dimension, wavelet analysis, Gabor, LBP, DFT, DCT, Laws masks, edge histogram and GLCM	Calcaneal (Manual)	58 cases &58 controls	RF	74.1	74.1	–	–	74.1	–	Zheng and Makrogiannis (2016)
4	1D projection modeled as fractional Brownian motion	Calcaneal (Manual)	–	SVM	96.9	97.6	–	–	94.5	94.3	Tafraouti et al. (2017)
5	Fractional Brownian model and Rao geodesic distance	Calcaneal	348 cases &348 controls	KNN	97.8	95.4	–	–	96.6	96.5	El Hassouni et al. (2017)
6	Histogram and GLCM and PCA analysis	Calcaneal (Manual)	87 cases &87 controls	SVM	97.7	95.4	95.5	97.7	96.6	96.6	Singh et al. (2017)
7	Anisotropic discrete dual-tree wavelet transform	Calcaneal (Manual)	87 cases &87 controls	SVM	–	93.1	92.9	91.0	91.9	91.9	Oulhaj et al. (2017a)
8	Wavelet decomposition and parametric circular models	Calcaneal (Manual)	87 cases &87 controls	SVM	100	92.5	91.9	100	95.9	95.8	Oulhaj et al. (2017b)
9	Oriental fractal analysis	Calcaneal (Manual)	87 cases &87 controls	–	72.0	71.0	72.0	71.0	71.8	72.2	Harrar et al. (2018)
10	BMD, fractal, histomorphometric and skeletal measures	Distal radius	47 cases &47 controls	SVM	79.0	66.0	–	–	–	–	Lee et al. (2008)
11	Proposed method	Distal radius (Automated)	60 cases &60 controls								
(a)	Cortical, histogram, GLCM and MGM			SVM	86.7	65.0	71.2	83.0	75.8	78.2	
(b)	Cortical and LLBP			SVM	88.3	66.7	72.6	85.1	77.5	79.7	
(c)	Cortical and hLLBP			LR	81.7	76.7	77.8	80.7	79.2	79.7	
(d)	Cortical and vLLBP			SVM	88.3	60.0	68.8	83.7	74.2	77.4	

hLLBP and vLLBP – horizontal and vertical LLBP; LR – Logistic regression; RF – Random Forest.

Conflict of interest

The authors declare that they have no conflict of interest.

Acknowledgements

We thank the Institutional Scientific and Ethical Committee, Kasturba Medical College (KMC) Hospital, Mangalore, Manipal Academy of Higher Education, Karnataka, India for approving the study protocol. We also thank the Department of Orthopedics, District Wenlock Hospital, Mangalore, Karnataka, India and Tejaswini Hospital, Mangalore, Karnataka, India for the help and support extended towards the data collection. We would like to thank the University Hospital of Geneva (HUG), Geneva, Switzerland for the data provided. We also thank the International Office, Haute Ecole d'Ingenierie et de Gestion du Canton de Vaud (HEIG-VD), Yverdon-les-Bains, Switzerland and the Centre of Biomedical Imaging (CIBM), HUG, Geneva, Switzerland for the opportunity, help and support provided. We would also like to thank and acknowledge Dr. Nikil Jayasheelan (Department of Orthopedics, KMC, India), Dr. Francois Lazeyras (Division of Radiology, Department of Radiology and Medical Informatics, HUG, Switzerland), Dr. Jean-Pierre Willi, Dr. Osman Ratib and Mr. Giulio Conicella (Division of Nuclear Medicine and Molecular Imaging, Department of Radiology and Medical Informatics, HUG, Switzerland) for their help and support extended to this work.

References

Adami, S., Zamberlan, N., Gatti, D., Zanfisi, C., Braga, V., Broggini, M., Rossini, M., 1996. Computed radiographic absorptiometry and morphometry in the assessment of postmenopausal bone loss. Osteoporos. Int. 6, 8–13.

Anburajan, M., Rethinasabapathi, C., Korath, M.P., Ponnappa, B., Panicker, T., Govindan, A., Prasad, G., Evans, W., Jagadeesan, K., 2001. Low cost mass screening tool for evaluating post-menopausal osteoporosis: a breakthrough for the developing world. Bombay Hosp. J. 43, 53–60.

Areeckal, A.S., Jayasheelan, N., Kamath, J., Zawadynski, S., Kocher, M., David, S.S., 2018a. Early diagnosis of osteoporosis using radiogrammetry and texture analysis from hand and wrist radiographs in Indian population. Osteoporos. Int. 29, 665–673.

Areeckal, A.S., Sam, M., David, S.S., 2018b. Computerized radiogrammetry of third metacarpal using watershed and active appearance model. In: Proc. 19th Int. Conf. Industrial Technol. (ICIT). IEEE. pp. 1490–1495.

Barnett, E., Nordin, B., 1960. The radiological diagnosis of osteoporosis: a new approach. Clin. Radiol. 11, 166–174.

Böttcher, J., Malich, A., Pfeil, A., Petrovitch, A., Lehmann, G., Heyne, J., Hein, G., Kaiser, W., 2004. Potential clinical relevance of digital radiogrammetry for quantification of periarticular bone demineralization in patients suffering from rheumatoid arthritis depending on severity and compared with DXA. Eur. Radiol. 14, 631–637.

Dabov, K., Foi, A., Katkovnik, V., Egiazarian, K., 2007. Image denoising by sparse 3-D transform-domain collaborative filtering. IEEE Trans. Image Process. 16, 2080–2095.

Dendere, R., Kabelitz, G., Douglas, T.S., 2013. Model-based segmentation of the middle phalanx in digital radiographic images of the hand. In: 35th Annual International Conference of the IEEE Engineering in Medicine and Biology Society (EMBC). IEEE. pp. 3702–3705.

Dougherty, E.R., Lotufo, R.A., 2003. Hands-on Morphological Image Processing for Optical Engineering SPIE, T.I.S., vol. 71. SPIE Optical Engineering Press, Washington.

El Hassani, A.S., El Hassouni, M., Houam, L., Rziza, M., Lespessailles, E., Jennane, R., 2012. Texture analysis using dual tree M-band and Rényi entropy: application to osteoporosis diagnosis on bone radiographs. In: 9th IEEE International Symposium on Biomedical Imaging (ISBI). IEEE. pp. 1487–1490.

El Hassouni, M., Tafraouti, A., Toumi, H., Lespessailles, E., Jennane, R., 2017. Fractional Brownian motion and Rao geodesic distance for bone X-Ray image characterization. IEEE J. Biomed. Health Inform. 21, 1347–1359.

Fischer, L., 2009. Using shape particle filters for robust medical image segmentation. Technical Report. Vienna University of Technology.

Gomberg, B.R., Saha, P.K., Wehrli, F.W., 2003. Topology-based orientation analysis of trabecular bone networks. Med. Phys. 30, 158–168.

Haralick, R.M., 1979. Statistical and structural approaches to texture. Proceedings of the IEEE 67, 786–880.

Harrar, K., Jennane, R., Zaouchi, K., Janvier, T., Toumi, H., Lespessailles, E., 2018. Oriented fractal analysis for improved bone microarchitecture characterization. Biomed. Signal Process. Control 39, 474–485.

Houam, L., Hafiane, A., Boukrouche, A., Lespessailles, E., Jennane, R., 2014. One dimensional local binary pattern for bone texture characterization. Pattern Anal. Appl. 17, 179–193.

Hui, S.L., Gao, S., Zhou, X.H., Johnston, C.C., Lu, Y., Glüer, C.C., Grampp, S., Genant, H., 1997. Universal standardization of bone density measurements: a method with optimal properties for calibration among several instruments. J. Bone Miner. Res. 12,

1463–1470.
IOF, 2013. Asia-Pacific Regional Audit on Epidemiology, Costs and Burden of Osteoporosis in 2013. Technical Report. IOF Regionals 4th Asia-Pacific Osteoporosis Meeting, Hong Kong.
Jennane, R., Touvier, J., Bergounioux, M., Lespessailles, E., 2014. A variational model for trabecular bone radiograph characterization. In: IEEE 11th International Symposium on Biomedical Imaging (ISBI). IEEE. pp. 1283–1286.
Langs, G., Peloschek, P., Donner, R., Reiter, M., Bischof, H., 2006. Active feature models. In: 18th International Conference on Pattern Recognition (ICPR). IEEE. pp. 417–420.
Lee, S., Lee, J.W., Jeong, J.W., Yoo, D.S., Kim, S., 2008. A preliminary study on discrimination of osteoporotic fractured group from nonfractured group using support vector machine. In: IEEE 30th Annual International Conference of the IEEE Engineering in Medicine and Biology Society (EMBS). IEEE. pp. 474–477.
Lespessailles, E., Gadois, C., Kousignian, I., Neveu, J., Fardellone, P., Kolta, S., Roux, C., Do-Huu, J., Benhamou, C., 2008. Clinical interest of bone texture analysis in osteoporosis: a case control multicenter study. Osteoporos. Int. 19, 1019–1028.
Lu, Y., Fuerst, T., Hui, S., Genant, H., 2001. Standardization of bone mineral density at femoral neck, trochanter and Ward's triangle. Osteoporos. Int. 12, 438–444.
Majumdar, S., Link, T.M., Millard, J., Lin, J.C., Augat, P., Newitt, D., Lane, N., Genant, H.K., 2000. In vivo assessment of trabecular bone structure using fractal analysis of distal radius radiographs. Med. Phys. 27, 2594–2599.
Mallard, F., Bouvard, B., Mercier, P., Bizot, P., Cronier, P., Chappard, D., 2013. Trabecular microarchitecture in established osteoporosis: relationship between vertebrae, distal radius and calcaneus by X-ray imaging texture analysis. Orthop. Traumatol.: Surg. Res. 99, 52–59.
Mccreadie, B.R., Goldstein, S.A., 2000. Biomechanics of fracture: is bone mineral density sufficient to assess risk? J. Bone Miner. Res. 15, 2305–2308.
Ojala, T., Pietikainen, M., Maenpaa, T., 2002. Multiresolution gray-scale and rotation invariant texture classification with local binary patterns. IEEE Trans. Pattern Anal. Mach. Intell. 24, 971–987.
Oulhaj, H., Rziza, M., Amine, A., Toumi, H., Lespessailles, E., El Hassouni, M., Jennane, R., 2017a. Anisotropic discrete dual-tree wavelet transform for improved classification of trabecular bone. IEEE Trans. Med. Imaging 36, 2077–2086.
Oulhaj, H., Rziza, M., Amine, A., Toumi, H., Lespessailles, E., Jennane, R., El Hassouni, M., 2017b. Trabecular bone characterization using circular parametric models. Biomed. Signal Process. Control 33, 411–421.
Pande, K.C., Veeraji, E., Pande, S.K., 2006. Normative reference database for bone mineral density in Indian men and women using digital X-ray radiogrammetry. J. Indian Med. Assoc. 104, 288–291.
Petpon, A., Srisuk, S., 2009. Face recognition with local line binary pattern. In: Fifth International Conference on Image and Graphics (ICIG'09). IEEE. pp. 533–539.
Raheja, A.J., 2008. Automated analysis of metacarpal cortical thickness in serial hand radiographs, Ph. D. thesis. Wright State University.
Rosholm, A., Hyldstrup, L., Baeksgaard, L., Grunkin, M., Thodberg, H., 2001. Estimation of bone mineral density by digital X-ray radiogrammetry: theoretical background and clinical testing. Osteoporos. Int. 12, 961–969.
Sam, M., Areeckal, A.S., David, S.S., 2017. Early diagnosis of osteoporosis using active appearance model and metacarpal radiogrammetry. In: Proc. 13th Int. Conf. Signal-Image Technol. and Internet-Based Syst. (SITIS). IEEE. pp. 173–178.
Seo, G.S., Shiraki, M., Aoki, C., Chen, J.T., Aoki, J., Imose, K., Togawa, Y., Inoue, T., 1994. Assessment of bone density in the distal radius with computer assisted X-ray densitometry (CXD). Bone Miner. 27, 173–182.
Shankar, N., Sapthagirivasan, V., Vijay, A., Kirthika, K., Anburajan, M., 2010. Evaluation of osteoporosis using radiographic hip geometry, compared with dual energy X-ray absorptiometry (DXA) as the standard. In: International Conference on Systems in Medicine and Biology (ICSMB). IEEE. pp. 259–264.
Singh, A., Dutta, M.K., Jennane, R., Lespessailles, E., 2017. Classification of the trabecular bone structure of osteoporotic patients using machine vision. Comput. Biol. Med. 91, 148–158.
Tafraouti, A., El Hassouni, M., Toumi, H., Lespessailles, E., Jennane, R., 2017. Osteoporosis diagnosis using frequency separation and fractional Brownian motion. In: Proc. Int. Conf. on Wireless Networks and Mobile Communications (WINCOM). IEEE. pp. 1–4.
Thodberg, H., Van Rijn, R., Tanaka, T., Martin, D., Kreiborg, S., 2010. A paediatric bone index derived by automated radiogrammetry. Osteoporos. Int. 21, 1391–1400.
Thodberg, H.H., Rosholm, A., 2003. Application of the active shape model in a commercial medical device for bone densitometry. Image Vis. Comput. 21, 1155–1161.
Touvier, J., Winzenrieth, R., Johansson, H., Roux, J., Chaintreuil, J., Toumi, H., Jennane, R., Hans, D., Lespessailles, E., 2015. Fracture discrimination by combined bone mineral density (BMD) and microarchitectural texture analysis. Calcified Tissue Int. 96, 274–283.
Veenland, J., 1999. Texture analysis of the radiographic trabecular bone pattern in osteoporosis. Ph. D. thesis. Erasmus University, Rotterdam.
Vokes, T., Lauderdale, D., Ma, S.L., Chinander, M., Childs, K., Giger, M., 2010. Radiographic texture analysis of densitometric calcaneal images: relationship to clinical characteristics and to bone fragility. J. Bone Miner. Res. 25, 56–63.
Ward, K., Cotton, J., Adams, J., 2003. A technical and clinical evaluation of digital X-ray radiogrammetry. Osteoporos. Int. 14, 389–395.
Werman, M., Peleg, S., 1984. Multiresolution texture signatures using min–max operators. Seventh International Conference on Pattern Recognition 97–101.
WHO, 2007. Assessment of osteoporosis at the primary health care level. Summary Report of a WHO Scientific Group. Technical Report. WHO Scientific Group, WHO, Geneva.
Wigderowitz, C., Paterson, C., Dashti, H., McGurty, D., Rowley, D., 2000. Prediction of bone strength from cancellous structure of the distal radius: can we improve on DXA? Osteoporos. Int. 11, 840–846.
Yger, F., 2014. Challenge IEEE-ISBI/TCB: Application of covariance matrices and wavelet marginals. arXiv preprint arXiv:1410.2663.
Zheng, K., Makrogiannis, S., 2016. Bone texture characterization for osteoporosis diagnosis using digital radiography. In: IEEE 38th Annual International Conference of the Engineering in Medicine and Biology Society (EMBC). IEEE. pp. 1034–1037.